LBNL-56656

Shadowing and Absorption Effects on J/ψ Production in dA Collisions

R. Vogt
Nuclear Science Division, Lawrence Berkeley National Laboratory, Berkeley, CA 94720, USA
and
Physics Department, University of California, Davis, CA 95616, USA

Abstract

We study medium modifications of J/ψ production in cold nuclear media in deuterium-nucleus collisions. We discuss several parameterizations of the modifications of the parton densities in the nucleus, known as shadowing, an initial-state effect. We also include absorption of the produced J/ψ by nucleons, a final-state effect. Both spatially homogeneous and inhomogeneous shadowing and absorption are considered. We use the number of binary nucleon-nucleon collisions as a centrality measure. Results are presented for d+Au collisions at $\sqrt{S_{NN}} = 200$ GeV and for d+Pb collisions at $\sqrt{S_{NN}} = 6.2$ TeV. To contrast the centrality dependence in pA and dA collisions, we also present pPb results at $\sqrt{S_{NN}} = 8.8$ TeV.

The nuclear, or A, dependence of J/ψ production is an important topic of study for nuclear collisions. It is essential that the A dependence be understood in cold nuclear matter to set a proper baseline for quarkonium suppression in AA collisions. At fixed target energies, NA50 [1] has studied the J/ψ A dependence and attributed its behavior to J/ψ break up by nucleons in the final state, referred to as nuclear absorption. However, it is also known that the parton distributions are modified in the nucleus relative to free protons. This modification, referred to here as shadowing, is increasingly important at higher energies. This paper studies the interplay of shadowing and absorption in deuteron-gold collisions at the Relativistic Heavy Ion Collider (RHIC) and in deuteron-lead and proton-lead collisions at the future Large Hadron Collider (LHC). We consider both spatially homogeneous (minimum bias collisions) and inhomogeneous (fixed impact parameter) results. When possible, we discuss the results in the context of data, in particular, the PHENIX data from RHIC.

The nuclear quark and antiquark distributions have been probed through deep inelastic scattering (DIS) of leptons and neutrinos from nuclei. These experiments showed that parton densities in nuclei are modified relative to those in free protons [2]. It has been shown that diffraction and shadowing arise from final-state interactions in DIS. Since shadowing results from diffractive processes in the Glauber formalism, nuclear shadowing is not an intrinsic property of the nuclear wavefunction in isolation [3]. To describe the effects of shadowing, we use parameterizations of the nuclear parton densities derived from fits to data.

These parameterizations have three basic momentum fraction, x, regimes. At low parton momentum fractions, $x < 0.02$, the ratio of the nuclear parton density relative to the nucleon is less than unity (shadowing). In the intermediate x regime, $0.02 < x < 0.1$, this ratio is larger than unity (antishadowing) while at higher x it drops below unity once more (EMC region). The effect also depends on the scale of the interaction, the square of the momentum transfer, Q^2. As the collision energy increases, the x values probed are decreased, making shadowing more important. Since shadowing affects the parton distribution functions before the parton-parton collision that produces the J/ψ occurs, we refer to it here as an initial state effect.

Shadowing should depend on the spatial position of the interacting parton within the nucleus [4]. Although DIS experiments are typically insensitive to this position dependence, some spatial inhomogeneity has been observed in νN scattering [5]. Thus the effect should be sensitive to the impact parameter, b, at which the collision occurs so that the results depend on the collision centrality. Central collisions with low impact parameter should exhibit stronger shadowing effects than collisions in the nuclear periphery. In Refs. [4,6], we discussed the effects of spatially inhomogeneous shadowing on J/ψ production in AA and dA collisions respectively. In this paper, we augment the dA predictions by including final-state absorption of the J/ψ by nucleons.

At lower fixed-target energies, such as those at the CERN SPS, the x values are rather high, $x \sim 0.18$ at midrapidity, and shadowing effects are small. In this energy and rapidity regime, the A dependence of J/ψ production is typically attributed to nuclear absorption of the J/ψ: either the pre-resonant $c\bar{c}$ pair or the J/ψ itself can interact with nucleons along its path and break up into charm hadrons in reactions such as $pJ/\psi \to D\overline{D}X$ or $pJ/\psi \to \overline{D}\Lambda_c$. However, at energies such as those available at RHIC and the LHC, especially away from midrapidity, much smaller x values may be reached, making shadowing more important relative to absorption.

The $c\bar{c}$ pair that produces the J/ψ can be created in either color singlet or color octet states. In Ref. [7], absorption was described in terms of the singlet and octet components of the J/ψ wavefunction,

$$|J/\psi\rangle = a_0|(c\bar{c})_1\rangle + a_1|(c\bar{c})_8 g\rangle + a_2|(c\bar{c})_1 gg\rangle + a_2'|(c\bar{c})_8 gg\rangle + \cdots . \quad (1)$$

In the color singlet model [8], only the first component is nonzero for direct J/ψ production. The $c\bar{c}$ pairs pass through nuclear matter in small color singlet states and reach their bound state size outside the nucleus, except at sufficiently negative rapidity where the J/ψ may still hadronize inside the nuclear medium. If $c\bar{c}$ pairs are predominantly produced in color octet states, then the $|(c\bar{c})_8 g\rangle$ state interacts with nucleons. The produced color octet $c\bar{c}$ can neutralize its color by a nonperturbative interaction with a gluon. Since the $|(c\bar{c})_8 g\rangle$ state is fragile, a gluon exchange between it and a nucleon would separate the $(c\bar{c})_8$ from the gluon and break up the unbound octet [7]. If the $|(c\bar{c})_8 g\rangle$ state evolves without interaction, such as in pp collisions, the additional gluon is absorbed by the octet $c\bar{c}$ pair, hence 'evaporating' the color. The color evaporation model (CEM) thence does not care about the relative coefficients in Eq. (1) and treats all $c\bar{c}$ pairs with masses less than twice the D meson mass identically. The CEM can successfully reproduce the quarkonium transverse momentum, p_T, dependence at collider energies. It also predicts no polarization, consistent with available data [9]. On the other hand, the NRQCD approach, applied to the total cross section in

Ref. [10], provides the leading coefficients in the expansion of the wavefunction in Eq. (1), encompassing both singlet and octet production and absorption. While NRQCD also gives a good description of the Tevatron quarkonium p_T distributions, it so far cannot describe the quarkonium polarization [9]. It also cannot explain the BELLE $J/\psi + \eta_c$ result [11]. To compare results in both approaches, we calculate absorption of color singlets and color octets in the CEM as well as the combination of the two in NRQCD. The NRQCD approach fixes the fraction of charmonium states produced in color singlets and color octets, determining the rate of singlet and octet absorption in Eq. (1).

The nuclear dependence of hard process production such as heavy quarks and quarkonium in AB collisions is typically parameterized as

$$\sigma_{AB} = \sigma_{NN}(AB)^{\alpha} \tag{2}$$

where A and B can be either protons or nuclei and σ_{NN} is the production cross section in a nucleon-nucleon collision. At central values of rapidity, y, or Feynman x, x_F, where $x_F = 2p_z/\sqrt{S_{NN}} = 2m_T \sinh y/\sqrt{S_{NN}}$, $m_T = \sqrt{p_T^2 + m^2}$ where p_T is the transverse momentum and m is the particle mass, the A dependence of open charm production is, to a good approximation, linear with $\alpha = 1$ [12]. However, for quarkonium production, $\alpha < 1$ at midrapidity. The most recent measurements by experiment E866 at Fermilab [13] and NA50 at CERN [1] suggest $\alpha \sim 0.94 - 0.95$ at $x_F \sim 0$. Dependence on the kinematic variables x_F and p_T has been observed. Typically $\alpha(x_F)$ decreases with increasing x_F at $x_F > 0$. Little data is available for $x_F \leq -0.1$ so that the behavior in this region is not well known experimentally.

It is as yet unknown if α is a strong function of energy, as predicted by some absorption models [14,15]. If color singlet absorption is at work, the absorption contribution should decrease with energy because the singlet state will stay small until far outside the target [14]. On the other hand, if the absorption cross section depends on the NJ/ψ center of mass energy, at higher values of $\sqrt{S_{NN}}$ the average NJ/ψ center of mass energy increases, thus increasing the absorption cross section [15]. Since both initial and final-state effects such as shadowing and absorption may be dependent on $\sqrt{S_{NN}}$, empirically it would seem that α should be energy dependent. At low energies, most analyses have assumed that absorption by nucleons is the only contribution to the A dependence. While this may be a good approximation at midrapidity, measured by NA50, away from the central region α is x_F dependent, as previously mentioned. Thus absorption alone is not enough to explain the x_F dependence, as already noted a number of times, see *e.g.* Refs. [16–18].

Indeed, the characteristic shape of $\alpha(x_F)$ at high x_F, $x_F \geq 0.25$, also cannot be explained by shadowing alone [16]. In fact, the data demonstrate scaling with x_F, not x_2, the target momentum fraction, in contradiction to perturbative QCD factorization, indicating the possible importance of higher-twist effects [19]. Effects we have not considered here which may result in x_F rather than x_2 scaling and affect the high x_F region are energy loss in cold matter and intrinsic charm, both discussed extensively in Ref. [16]. We do not consider these effects because, at heavy ion colliders, the relationship between x_F, rapidity, and $\sqrt{S_{NN}}$ means that this interesting x_F region is pushed to very far forward rapidities, outside the measureable region. Energy loss effects, such as those considered in Ref. [16], using the Brodsky and Hoyer bound [20] with the Baier *et al.* formalism [21], become inapplicable for $\Delta x_1 > x_1$, occurring at $x_F \leq -0.017$ at $\sqrt{S_{NN}} = 200$ GeV. We have checked the effect of this energy

loss and found that the ratio dA/pp is essentially unity for $x_F > 0$. At $\sqrt{S_{NN}} = 200$ GeV and $y = 2.5$, the forward edges of the PHENIX muon arms at RHIC, $x_F \sim 0.19$ for a J/ψ with $p_T = 0$ while at $\sqrt{S_{NN}} = 5.5$ TeV and $y = 4$, the forward edge of the ALICE muon arm at the LHC, $x_F \sim 0.03$, both far from the region where intrinsic charm [22] is important. Therefore, at collider energies, a combination of absorption and shadowing effects may be sufficient to address the J/ψ data.

In this paper, we discuss the combined effects of shadowing and absorption both in minimum bias dA collisions and as a function of centrality at RHIC and the LHC. We focus on d+Au collisions at $\sqrt{S_{NN}} = 200$ GeV at RHIC and d+Pb collisions at $\sqrt{S_{NN}} = 6.2$ TeV at the LHC. While it is unclear whether pA or dA collisions will be used at the LHC, one advantage of dA is that the energy is closer to that of Pb+Pb collisions at $\sqrt{S_{NN}} = 5.5$ TeV whereas the p+Pb center of mass energy per nucleon would be 8.8 TeV. Thus the d+Pb combination has been suggested as a baseline measurement at the LHC [23].

Our J/ψ calculations generally employ the color evaporation model which treats all charmonium production identically to $c\bar{c}$ production below the $D\overline{D}$ threshold, neglecting color and spin [24]. The leading order (LO) rapidity distributions of J/ψ's produced in dA collisions at impact parameter b is

$$\frac{d\sigma}{dyd^2bd^2r} = 2F_{J/\psi}K_{\rm th}\int dzdz'\int_{2m_c}^{2m_D} MdM\left\{F_g^d(x_1,Q^2,\vec{r},z)F_g^A(x_2,Q^2,\vec{b}-\vec{r},z')\frac{\sigma_{gg}(Q^2)}{M^2}\right. \quad (3)$$

$$\left. + \sum_{q=u,d,s}[F_q^d(x_1,Q^2,\vec{r},z)F_{\overline{q}}^A(x_2,Q^2,\vec{b}-\vec{r},z') + F_{\overline{q}}^d(x_1,Q^2,\vec{r},z)F_q^A(x_2,Q^2,\vec{b}-\vec{r},z')]\frac{\sigma_{q\overline{q}}(Q^2)}{M^2}\right\} .$$

The partonic cross sections for LO gluon fusion and $q\overline{q}$ annihilation are given in Ref. [25], $M^2 = x_1x_2S_{NN}$ and $x_{1,2} = (M/\sqrt{S_{NN}})\exp(\pm y)$. The fraction of $c\bar{c}$ pairs below the $D\overline{D}$ threshold that become J/ψ's, $F_{J/\psi}$, is fixed at next-to-leading order (NLO) [24]. Both this fraction and the theoretical K factor, $K_{\rm th}$, which scales the LO cross section to the NLO value, drop out of the ratios. The K factor is independent of rapidity [26]. While our calculations are LO, the shadowing ratios are independent of the order of the calculation [6]. We use $m_c = 1.2$ GeV and $Q = M$ [24] with the MRST LO parton densities. We will compare our minimum bias CEM results with calculations employing the NRQCD approach and discuss any differences in the resulting shadowing and absorption patterns.

We assume that the nuclear parton densities, $F_j^A(x,Q^2,\vec{r},z)$, are the product of the nucleon density in the nucleus, $\rho_A(s)$, the nucleon parton density, $f_j^N(x,Q^2)$, and a shadowing ratio, $S_{\rm P,S}^j(A,x,Q^2,\vec{r},z)$, where $\vec{r}$ and z are the transverse and longitudinal location of the parton in position space. The first subscript, P, refers to the choice of shadowing parameterization, while the second, S, refers to the spatial dependence. Most available shadowing parameterizations, including the ones used here, ignore effects in deuterium. However, we take the proton and neutron numbers of both nuclei into account. Thus,

$$F_i^d(x,Q^2,\vec{r},z) = \rho_d(s)f_i^N(x,Q^2) \quad (4)$$

$$F_j^A(x,Q^2,\vec{b}-\vec{r},z') = \rho_A(s')S_{\rm P,S}^j(A,x,Q^2,\vec{b}-\vec{r},z')f_j^N(x,Q^2) , \quad (5)$$

where $s = \sqrt{r^2+z^2}$ and $s' = \sqrt{|\vec{b}-\vec{r}|^2+z'^2}$. With no nuclear modifications, $S_{\rm P,S}^i(A,x,Q^2,\vec{r},z) \equiv 1$. The nucleon densities of the heavy nucleus are assumed to be

Woods-Saxon distributions with $R_{\rm Au} = 6.38$ fm and $R_{\rm Pb} = 6.62$ fm [27]. We use the Húlthen wave function [28] to calculate the deuteron density distribution. The densities are normalized so that $\int d^2r dz \rho_A(s) = A$. We employ the MRST LO parton densities [29] for the free nucleon.

We have chosen shadowing parameterizations developed by two groups which cover extremes of gluon shadowing at low x. The Eskola *et al.* parameterization, EKS98, is based on the GRV LO [30] parton densities. Valence quark shadowing is identical for u and d quarks. Likewise, the shadowing of $\overline{u}$, $\overline{d}$ and $\overline{s}$ quarks are identical at Q_0^2. Shadowing of the heavier flavor sea quarks, $\overline{s}$ and higher, is, however, calculated and evolved separately at $Q^2 > Q_0^2$. The shadowing ratios for each parton type are evolved to LO for $1.5 < Q < 100$ GeV and are valid for $x \geq 10^{-6}$ [31,32]. Interpolation in nuclear mass number allows results to be obtained for any input A. The parameterizations by Frankfurt, Guzey and Strikman (FGSo, the original parameterization, along with FGSh and FGSl for high and low gluon shadowing) combine Gribov theory with hard diffraction [33]. They are based on the CTEQ5M [34] parton densities and evolve each parton species separately to NLO for $2 < Q < 100$ GeV. Although the x range is $10^{-5} < x < 0.95$, the sea quark and gluon ratios are unity for $x > 0.2$. The EKS98 valence quark shadowing ratios are used as input since Gribov theory does not predict valence shadowing. The FGSo parameterization is available for four different values of A: 16, 40, 110 and 206 while FGSh and FGSl also include $A = 197$. We use $A = 206$ for Au with FGSo and $A = 197$ for FGSh and FGSl.

Figure 1 compares the four homogeneous ratios, $S^j_{\rm EKS}$ and $S^j_{\rm FGSi}$ for $Q = 2m_c$. The FGS calculation predicts more shadowing at small x. The difference is especially large for gluons. At very low x, the gluon ratios for FGSo and FGSh are quite similar but in the intermediate x regime, the FGSh parameterization drops off more smoothly. On the other hand, the FGSl parameterization levels off at a higher value of $S^i_{\rm P}$ than the other two FGS parameterizations. In the antishadowing regime, FGSh and FGSl are rather similar to EKS98 while FGSo has a larger antishadowing effect. Obviously shadowing alone will give an effective A dependence as a function of rapidity with $y > 0$ corresponding to low x, effectively mirroring the curves in Fig. 1.

We note that it might be possible to rule out some parameterizations by comparing to predictions of cleaner final states at fixed-target energies, such as Drell-Yan lepton pair production. However, parton energy loss in cold matter may also affect Drell-Yan production [35]. As explained in Ref. [16], the Drell-Yan data at 800 GeV were included in the EKS98 parameterization, effectively excluding other effects. The FGS parameterizations did not include these data in their analyses and, as might be expected since gluon shadowing feeds into sea quark shadowing, leading to stronger than observed effects on Drell-Yan production. However, the possibility that some combination of shadowing and energy loss could be used to describe this data cannot be ruled out.

Figure 2 shows the average value of x_2, the fraction of the nucleon momentum carried by the interacting parton that produces the J/ψ, for pA collisions at the CERN SPS, $\sqrt{S_{NN}} = 19.4$ GeV, and dA collisions at RHIC, $\sqrt{S_{NN}} = 200$ GeV, and the LHC, $\sqrt{S_{NN}} = 6.2$ TeV. At midrapidity at the SPS, $\langle x_2 \rangle \sim 0.1$, in the antishadowing region. Note that if some level of antishadowing is indeed present at this energy, the effective absorption cross section determined from minimum bias pA data would actually be underestimated, as discussed in the context of Pb+Pb collisions in Ref. [36]. At midrapidity at RHIC, $\langle x_2 \rangle \sim 0.01$, near the

point where $S_{\rm P}^g \leq 1$. In the forward region, $\langle x_2 \rangle \sim 10^{-3}$ at $y \sim 2$, clearly in the effective low x regime due to gg dominance while for negative rapidity, $y \sim -2$, $\langle x_2 \rangle \sim 0.1$, in the antishadowing region. Even lower values of $\langle x_2 \rangle$ are reached in the measurable rapidity region of the LHC, at $y \sim 4$, $\langle x_2 \rangle \sim 10^{-5}$, deep in the shadowing region. Systematic studies over the widest possible $\langle x_2 \rangle$ range can map out the gluon distribution, especially for the nucleus, if absorption effects are understood.

We now turn to the spatial dependence of the shadowing, discussed in detail in Ref. [6]. Previously, when no inhomogeneous shadowing parameterizations were available, we considered two forms of the spatial dependence, one proportional to the local nuclear density, $S^j_{\rm P,WS}$, and the other proportional to the parton path through the nucleus, $S^j_{\rm P,\rho}$. Here we show only results for $S^j_{\rm P,\rho}$ and compare these to the results with the inhomogeneous FGS parameterizations, FGSh and FGSl. The $S^j_{\rm P,\rho}$ parameterization is, in general, [6]

$$S^j_{\rm P,\rho}(A,x,Q^2,\vec{r},z) = 1 + N_\rho(S^j_{\rm P}(A,x,Q^2) - 1)\frac{\int dz \rho_A(\vec{r},z)}{\int dz \rho_A(0,z)} \tag{6}$$

where N_ρ is chosen so that $(1/A)\int d^2r dz \rho_A(s) S^j_{\rm P,\rho}(A,x,Q^2,\vec{r},z) = S^j_{\rm P}(A,x,Q^2)$. When $s = \sqrt{r^2+z^2} \gg R_A$, the nucleons behave as free particles while the modifications are larger than the average value $S^j_{\rm P}(A,x,Q^2)$ in the center of the nucleus,. The normalization requires $(1/A)\int d^2r dz \rho_A(s) S^j_{\rm P,\rho} = S^j_{\rm P}$.

While there are three homogeneous FGS parameterizations, no spatial dependence is provided for FGSo, the case with the strongest gluon shadowing. Therefore, we also use $S^j_{\rm P,\rho}$ with this parameterization as well as with EKS98. The inhomogeneous FGSh and FGSl parameterizations are defined over $0.587 \leq s \leq 10$ fm for $A = 197$ and 208. Below $s_{\rm min} = 0.587$ fm, the ratios are fixed to those at $s_{\rm min}$ while $S^j_{\rm FGSh,l}(A,x,Q^2,\vec{s}) \to 1$ for $s \geq 10$ fm. They do not consider the longitudinal spatial dimension. The normalization requirement is similar to that of Eq. (6), $(1/A)\int d^2s T_A(s) S^j_{\rm FGSh,l}(A,x,Q^2,\vec{s}) = S^j_{\rm FGSh,l}(A,x,Q^2)$. Due to this fixed maximum, excluding the tail of the nuclear and deuteron density distributions, these parameterizations will have a somewhat stronger spatial dependence in a full dA calculation.

Figure 3 compares $S^j_{\rm FGSo,WS}$ and $S^j_{\rm FGSo,\rho}$ with $S^j_{\rm FGSh}(b)$ at similar values of the homogeneous shadowing ratios. We see that $S^j_{\rm FGSo,\rho}$ is quite compatible with the available FGS inhomogeneous parameterizations.

To implement nuclear absorption on J/ψ production in dA collisions, the production cross section in Eq. (3) is weighted by the survival probability, $S^{\rm abs}$, so that

$$S^{\rm abs}(\vec{b}-\vec{s},z') = \exp\left\{-\int_{z'}^{\infty} dz'' \rho_A(\vec{b}-\vec{s},z'')\sigma_{\rm abs}(z''-z')\right\} \tag{7}$$

where z' is the longitudinal production point, as in Eq. (5), and z'' is the point at which the state is absorbed. The nucleon absorption cross section, $\sigma_{\rm abs}$, typically depends on where the state is produced in the medium and how far it travels through nuclear matter. If absorption alone is active, *i.e.* $S^j_{\rm P,S} \equiv 1$, then an effective minimum bias A dependence is obtained after integrating Eqs. (3) and (7) over the spatial coordinates. If $S^{\rm abs} = 1$ also, $\sigma_{{\rm d}A} = 2A\sigma_{pN}$. When $S^{\rm abs} \neq 1$, $\sigma_{{\rm d}A} = 2A^\alpha \sigma_{pN}$ where, if $\sigma_{\rm abs}$ is a constant, independent of the production mechanism for a nucleus of $\rho_A = \rho_0 \theta(R_A - b)$,

$$\alpha = 1 - \frac{9\sigma_{\rm abs}}{16\pi r_0^2} \tag{8}$$

where $r_0 = 1.2$ fm. Although we assume absorption is only effective for the heavy nucleus, the spatial dependence of the deuteron wavefunction is included in Eq. (3). The impact parameter dependence of absorption alone is shown in Fig. 4 for $\sigma_{\rm abs} = 3$ mb for a constant octet cross section, independent of rapidity, and color singlet absorption at $y = -2$ where the J/ψ can still hadronize in the target at $\sqrt{S_{NN}} = 200$ GeV. The minimum bias results are indicated by the dotted lines. Absorption is stronger at central impact parameters but dies away gradually at large values of b due to the long tails of the density distributions, particularly of deuterium.

The observed J/ψ yield includes feed down from χ_{cJ} and ψ' decays, giving

$$S^{\rm abs}_{J/\psi}(\vec{b}-\vec{s},z') = 0.58 S^{\rm abs}_{J/\psi,\,\rm dir}(\vec{b}-\vec{s},z') + 0.3 S^{\rm abs}_{\chi_{cJ}}(\vec{b}-\vec{s},z') + 0.12 S^{\rm abs}_{\psi'}(\vec{b}-\vec{s},z') \; . \tag{9}$$

As discussed previously, in color singlet production, the final state absorption cross section depends on the size of the $c\bar{c}$ pair as it traverses the nucleus, allowing absorption to be effective only while the cross section is growing toward its asymptotic size inside the target. On the other hand, if the $c\bar{c}$ is produced as a color octet, hadronization will occur only after the pair has traversed the target except at very backward rapidity. We have considered a constant octet cross section, as well as one that reverts to a color singlet at backward rapidities. For singlets, $S^{\rm abs}_{J/\psi,\,\rm dir} \neq S^{\rm abs}_{\chi_{cJ}} \neq S^{\rm abs}_{\psi'}$ since $\sigma^{\psi'}_{\rm abs} > \sigma^{\chi_c}_{\rm abs} > \sigma^{J/\psi}_{\rm abs}$ but, with octets, one assumes that $S^{\rm abs}_{J/\psi,\,\rm dir} = S^{\rm abs}_{\chi_{cJ}} = S^{\rm abs}_{\psi'}$ since the asymptotic absorption cross section is predicted to be equal for all charmonium states. Finally, we have also considered a combination of octet and singlet absorption in the context of NRQCD. See Ref. [37] for a detailed description of all the absorption models discussed.

The left-hand side of Fig. 5 shows EKS98 shadowing combined with the absorption models described in the text in minimum bias d+Au collisions at $\sqrt{S_{NN}} = 200$ GeV. The difference between the constant and growing octet cross sections is quite small at large $\sqrt{S_{NN}}$ with only a minor octet-to-singlet conversion effect at $y < -2$. Color singlet absorption is also important only at similar negative rapidities and is otherwise not different from shadowing alone. The relative combination of nonperturbative singlet and octet contributions in NRQCD changes the shape of the shadowing ratio slightly. The large χ_{cJ} singlet feed down contribution reduces the overall absorption effect on inclusive J/ψ production. Octet to singlet conversion, together with singlet absorption, can be observed at $y < -2$ as in the other cases.

Several values of the asymptotic absorption cross section, $\sigma_{\rm abs} = 1$, 3 and 5 mb, corresponding to $\alpha = 0.98$, 0.95 and 0.92 respectively using Eq. (9) are shown in Fig. 5. These values of $\sigma_{\rm abs}$ are somewhat smaller than those obtained for the sharp sphere approximation in Eq. (8). The diffuse surface of a real nucleus and the longer range of the density distribution results in a smaller value of $\sigma_{\rm abs}$ than that found for a sharp sphere nucleus. There is good agreement with the trend of the preliminary PHENIX data [38] for $\sigma_{\rm abs} = 0-3$ mb. We use a value of 3 mb in our further calculations to illustrate the relative importance of absorption and shadowing.

The right-hand side of Fig. 5 compares the EKS98 and FGS parameterizations, all with a growing octet cross section with an asymptotic value of $\sigma_{\rm abs} = 3$ mb. In the region that

PHENIX can measure, the EKS98 and FGSl results are essentially indistinguishable. The FGSh result lies between the FGSo and EKS98 results at forward rapidity but is also quite similar to EKS98 at negative rapidity.

Figure 6 shows the same calculations for d+Pb collisions at $\sqrt{S_{NN}} = 6.2$ TeV at the LHC. Although we have plotted the results relative to pp at the same energy, there are currently no plans to run LHC pp collisions at energies lower than 14 TeV. Short, lower energy proton runs might better establish the energy excitation functions for other processes so this possibility is not excluded. In any case, there should be sufficient 14 TeV data to produce a high statistics J/ψ baseline at this energy. Between the Tevatron Run II data at 1.96 TeV and the forthcoming LHC pp data at 14 TeV, it should be possible extrapolate to 6.2 TeV with relative accuracy.

In addition, it will not be possible to directly compare these results to LHC data unless the entire J/ψ p_T spectrum can be measured since these calculations are integrated over p_T. Tevatron Run II has shown that it is possible to measure the entire J/ψ p_T distribution at collider energies. A minimum p_T cut would reduce the amount of shadowing due to the Q^2 dependence.

At 6.2 TeV, the difference between the constant and growing octet cross sections is negligible for all rapidities shown while only a small absorption effect is seen for the color singlet model at $y < -5$. On the other hand, the difference between the shadowing parameterizations is larger. Indeed, for $y > 2$ there is nearly a factor of two difference between the EKS98 and FGS ratios, 0.5 and 0.25 respectively. This difference should be measurable in the ALICE muon arm, covering the region $2.5 < y < 4$. The results at negative rapidity are harder to discriminate since the difference between the shadowing ratios is decreased. As the antishadowing region is approached, around $y = -5$, the difference is almost negligible.

In central collisions, inhomogeneous shadowing is stronger than the homogeneous result. The stronger the homogeneous shadowing, the larger the inhomogeneity. In peripheral collisions, inhomogeneous effects are weaker than the homogeneous results but some shadowing is still present. Shadowing persists in part because the density in a heavy nucleus is large and approximately constant except close to the surface and also because the deuteron wave function has a long tail. We also expect absorption to be a stronger effect in central collisions. In Fig. 7, we show the inhomogeneous shadowing and absorption results for EKS98 and $\sigma_{\rm abs} = 3$ mb at $\sqrt{S_{NN}} = 200$ GeV as a function of b/R_A for the inhomogeneous to minimum bias ratio (dAu(b)/pp)/(dAu(ave)/pp) $\equiv$dAu(b)/dAu(ave), shown on the left-hand side. The ratios are shown for several values of rapidity to represent the behavior in the anti-shadowing (large negative y), shadowing (large positive y) and transition (midrapidity) regions. The ratios are all less than unity for $b/R_A < 0.7$, with stronger than average shadowing and absorption, and rise above unity for large b/R_A, weaker than average shadowing and absorption.

We note that for both color octet and color singlet production and absorption, the spatial dependence of the absorption, shown in Fig. 4, is weaker than the effect due to inhomogeneous shadowing at $x \sim 5 \times 10^{-4}$ in Fig. 3. The inhomogeneous shadowing effect has a stronger y dependence than absorption which, at collider energies, as illustrated in Figs. 5 and 6, is independent of y except at large, negative rapidity. This y-independence can help disentangle the effects of shadowing and absorption as a function of centrality. For example, if the b dependence of the dAu/pp ratio at RHIC could be determined at

$y \sim -0.5$, where the result with $\sigma_{\rm abs} = 0$, shown in Fig. 5, indicates dAu/$pp \sim 1$, the effect of absorption alone could be fixed for all measurable y, allowing the effect of shadowing alone to be determined for other values of y.

The right-hand side of Fig. 7 shows the dAu/pp ratios for the same rapidity values as a function of the number of binary NN collisions, $N_{\rm coll}$,

$$N_{\rm coll}(b) = \sigma_{NN}^{\rm in} \int d^2s T_A(s) T_B(|\vec{b} - \vec{s}|)$$

where T_A and T_B are the nuclear thickness functions and $\sigma_{NN}^{\rm in}$ is the inelastic nucleon-nucleon cross section, 42 mb at RHIC.

The dependence of the ratios on $N_{\rm coll}$ is almost linear. We do not show results for $N_{\rm coll} < 1$, corresponding to $b/R_A > 1.3$ on the left-hand side, the point where the dAu(b)/dAu(ave) ratios begin to flatten out. The weakest $N_{\rm coll}$ dependence occurs in the antishadowing region, illustrated by the $y = -2$ result (dot-dashed curve). The trends of the ratios as a function of $N_{\rm coll}$ are consistent with the PHENIX data from the north muon arm ($y = 2$) and the electron arms ($y = 0$) but the preliminary PHENIX results from the south arm ($y = -2$) are much stronger than our predictions and, in fact, go the opposite way. The overall dependence on $N_{\rm coll}$ is stronger than that obtained from shadowing alone, described in Ref. [6] where inhomogeneous shadowing effects depend strongly on the amount of homogeneous shadowing. Relatively large effects at low x are accompanied by the strongest b dependence. In the transition region around midrapidity at RHIC, the b dependence of the ratio dAu/pp due to shadowing is nearly negligible and almost all the $N_{\rm coll}$ dependence at $y \sim 0$ can be attributed to absorption. The effect of absorption alone as a function of $N_{\rm coll}$ is shown on the right-hand side of Fig. 4. The $y = -2$ results for color singlet production and absorption, in the antishadowing region, are fairly independent of $N_{\rm coll}$.

Figure 8 compares the EKS98 dAu/pp ratios as a function of $N_{\rm coll}$ to results with the FGS parameterizations for the same rapidities as in Fig. 7. Since EKS98 has the weakest low x shadowing, given the previous discussion it is not surprising that it also has the weakest dependence on $N_{\rm coll}$. The FGSo results have the strongest $N_{\rm coll}$ dependence due to its strongest overall shadowing. The FGSo ratio goes above unity at $y = -2$ since, even with a 3 mb absorption cross section, the minimum bias ratio is still greater than one at this rapidity. While the FGSh and FGSl minimum bias ratios are intermediate to the EKS98 and FGSo ratios, they are more similar to EKS98 at forward rapidities so that, especially for FGSl, the central results are quite similar to those of EKS98 at all rapidities. However, as b increases and $N_{\rm coll}$ decreases, they begin to differ. Since the FGSh and FGSl inhomogeneous parameterizations are tuned to become unity at 10 fm, the shadowing component vanishes as $N_{\rm coll} \to 1$. On the other hand, there is some residual absorption due to the overlapping tails of the deuteron and nuclear density distributions. Thus the $y = 0$ and $y = 2$ curves meet at $N_{\rm coll} = 1$. At still higher impact parameters, where $N_{\rm coll} < 1$, the $y = -2$ curve intersects the higher rapidity curves.

While shadowing alone is not incompatible with the preliminary minimum bias PHENIX data [38], some absorption should be present. The 3 mb color octet absorption cross section is also compatible with the minimum bias data [39] and gives reasonable agreement with the E866 data when shadowing and other effects important at forward x_F, discussed previously, are included [16]. After the data is binned in centrality, some discrimination between models may be possible. Including inhomogeneous absorption steepens the dependence on $N_{\rm coll}$ more

than with shadowing alone [6]. The preliminary PHENIX centrality dependence [38] seems to be relatively flat for the central electron arms and the north muon arm (positive rapidity) while the centrality dependence in the south muon arm (negative rapidity) seems to increase strongly with $N_{\rm coll}$. The EKS98 and FGSl calculations are most compatible with the central and north muon arm data while FGSo and FGSh seem somewhat too strong relative to the data. Perhaps with a smaller absorption cross section, these calculations could be made more compatible with the data. None of the calculations agree with the preliminary south muon arm data, exhibiting very little dependence on $N_{\rm coll}$. The final PHENIX data as well as any data from a future d+Au run would help better determine both the amount of gluon shadowing as well as the relative contributions of shadowing and absorption, both in minimum bias collisions and as a function of centrality. It may be that the PHENIX data would be more compatible with color singlet rather than color octet absorption although this would contradict fixed target results at $x_F \sim 0$ where shadowing is weak [1,13].

In Figs. 9 and 10 we present our inhomogeneous shadowing and absorption calculations for d+Pb collisions at $\sqrt{S_{NN}} = 6.2$ TeV at the LHC. Figure 9 shows only the EKS98 results while Fig. 10 compares the EKS98 results as a function of $N_{\rm coll}$ to those of FGS. Here we have also included results for $y = \pm 4$, within the range of the ALICE muon arm. Given that the rapidity range of the muon arm encompasses the crossover point where dPb/$pp \sim 1$ at $y \sim -3.9$, the centrality dependence of absorption alone could be determined and used to calibrate the inhomogeneous shadowing effects. Note that it is only possible to reach $y \sim -3.9$ in ALICE by switching the beam directions and running Pb+d since the muon arm is only on one side of midrapidity. Both ALICE and CMS should be able to measure J/ψ production at $y = \pm 2$ and 0. Since the exact pp baseline is likely to be absent, as discussed above, perhaps a better baseline for the centrality dependence would be the ratio relative to the minimum bias result, shown on the left-hand side of Fig. 9 as a function of b/R_A. The change in dPb(b)/dPb(ave) with b/R_A at the LHC is stronger than that of dAu(b)/dAu(ave) at RHIC, shown in Fig. 7.

The results for $y = 4$, ± 2 and 0, all in the low x shadowing region, are rather closely grouped together. This should not be surprising because the EKS98 shadowing ratios shown in Fig. 6 are not very strong functions of rapidity. The grouping of the results is even more striking as a function of $N_{\rm coll}$, shown on the right-hand side of Fig. 9. Note also here that the x-axis scale is expanded relative to that of RHIC since $\sigma^{\rm in}_{NN} = 76$ mb at 6.2 TeV, increasing the number of inelastic NN collisions possible at the LHC. The expanded $N_{\rm coll}$ scale also has implications for the FGSh and FGSl parameterizations with their sharp 10 fm cutoff on shadowing. As seen in Fig. 10(c) and (d), the curvature of these parameterizations is much stronger than the linear dependence produced by Eq. (6). This increased strength is due to the larger value of $\sigma^{\rm in}_{NN}$ at the LHC. Now $N_{\rm coll} \approx 1$ at $b \sim 10$ fm. Here FGSh and FGSl shadowing vanishes and the curves all come together at the value of the ratio corresponding to the amount of residual absorption. The curvature increases with y since the larger shadowing ratio has to increase to unity faster than those at negative rapidity where shadowing is weaker.

The results in Figs. 9 and 10 show that while, at $y \leq 0$ in Fig. 6 good statistical accuracy is necessary to discriminate between shadowing models, the difference in their $N_{\rm coll}$ dependence may be sufficient to do so.

Finally, since it is not yet clear whether proton or deuterium comparison runs will be

used at the LHC, Fig. 11 shows the results for p+Pb collisions at $\sqrt{S_{NN}} = 8.8$ TeV, the appropriate energy for proton-nucleus collisions. We have plotted the results assuming that the center of mass rapidity is at $y = 0$, as is the case for symmetric beams. However, since the charge-to-mass, Z/A, ratio is different for protons and lead, the proton beam has an energy of 7 TeV while the Pb beam has energy 2.75 TeV. The asymmetric energies lead to a shift of the center of mass rapidity of 0.5 units in the direction of the proton beam. Since the difference between the Z/A ratios of deuterium and lead is much smaller, the shift in d+Pb collisions is only 0.1 unit. The p+Pb antishadowing peak is shifted further toward negative rapidity while the region where the parameterizations flatten begins closer to midrapidity than in Fig. 6. Thus the EKS98 results as function of $N_{\rm coll}$, shown on the right-hand side of Fig. 11 for $y = 4$ (solid curve) and $y = 0$ (dashed curve) are quite close together: the shadowing ratio changes very little as a function of rapidity. The corresponding FGSh results are shown in the dot-dashed and dotted curves respectively. In both cases, the $N_{\rm coll}$ dependence is stronger than in d+Pb collisions, as exhibited by the disappearance of both shadowing and absorption as $N_{\rm coll} \to 1$ for the two inhomogeneous shadowing parameterizations. The change in slope is particularly strong for EKS98 because the proton is treated as a point particle while the deuteron is an extended system. The maximum $N_{\rm coll}$ for p+Pb is slightly larger than half that for d+Pb. If not for the higher inelastic cross section, $\sigma^{\rm in}_{NN} = 81$ mb at 8.8 TeV, $N_{\rm coll}$ in p+Pb would be exactly half that of d+Pb.

In conclusion, the preliminary PHENIX data show that J/ψ production in d+Au collision is modified with respect to production in pp collisions at the same energy. This modification is consistent with initial-state shadowing plus final-state absorption seen in fixed-target experiments at 800 GeV [16]. More precise measurements may help to better set the level of absorption allowed by the data. Precision measurements of the centrality dependence may also help. Corresponding data from the LHC will be more useful for separating and refining shadowing models due the very low x range available for large rapidity measurements.

We thank K.J. Eskola and V. Guzey for their shadowing parameterizations. We also thank S.R. Klein and M.J. Leitch for discussions. This work was supported in part by the Division of Nuclear Physics of the Office of High Energy and Nuclear Physics of the U.S. Department of Energy under Contract Number DE-AC03-76SF00098.

REFERENCES

[1] B. Alessandro *et al.* (NA50 Collaboration), Eur. Phys. J. C **33**, 31 (2004).

[2] J.J. Aubert *et al.*, Nucl. Phys. B **293**, 740 (1987); M. Arneodo, Phys. Rep. **240**, 301 (1994).

[3] S.J. Brodsky, P. Hoyer, N. Marchal, S. Peigne and F. Sannino, Phys. Rev. D **65**, 114025 (2002).

[4] V. Emel'yanov, A. Khodinov, S.R. Klein and R. Vogt, Phys. Rev. C **61**, 044904 (2000).

[5] T. Kitagaki *et al.*, Phys. Lett. B **214**, 281 (1988).

[6] S.R. Klein and R. Vogt, Phys. Rev. Lett. **91**, 142301 (2003).

[7] D. Kharzeev and H. Satz, Phys. Lett. B **366**, 316 (1996).

[8] R. Baier and R. Rückl, Z. Phys. C **19**, 251 (1983); G.A. Schuler, hep-ph/9403387, CERN-TH.7170/94.

[9] N. Brambilla *et al.* (Quarkonium Working Group), hep-ph/0412158.

[10] M. Beneke and I.Z. Rothstein, Phys. Rev. D **54**, 2005 (1996).

[11] A.E. Bondar and V.L. Chernyak, hep-ph/0412335.

[12] M.J. Leitch *et al.* (E789 Collaboration), Phys. Rev. Lett. **72**, 2542 (1994).

[13] M.J. Leitch *et al.* (E866 Collaboration), Phys. Rev. Lett. **84**, 3256 (2000).

[14] S. Gavin and R. Vogt, Nucl. Phys. B **345**, 104 (1990).

[15] M. Bedjidian *et al.*, hep-ph/0311048.

[16] R. Vogt, Phys. Rev. C **61**, 035203 (2000).

[17] R. Vogt, S.J. Brodsky, and P. Hoyer, Nucl. Phys. B **360**, 67 (1991).

[18] J. Hüfner and M. Simbel, Phys. Lett. B **258**, 465 (1991).

[19] P. Hoyer, M. Vänttinen and U. Sukhatme, Phys. Lett. B **246**, 217 (1990).

[20] S.J. Brodsky and P. Hoyer, Phys. Lett. B **298** 165, (1993).

[21] R. Baier, Yu.L. Dokshitzer, A.H. Mueller, S. Peigne, and D. Schiff, Nucl. Phys. B **484** 265, (1997); R. Baier, Yu.L. Dokshitzer, A.H. Mueller, and D. Schiff, Nucl. Phys. B **531** 403, (1998).

[22] S.J. Brodsky, P. Hoyer, C. Peterson, and N. Sakai, Phys. Lett. **B93** 451, (1980); S.J. Brodsky, C. Peterson, and N. Sakai, Phys. Rev. **D23** 2745, (1981).

[23] P. Carminati *et al.* (ALICE Collaboration), J. Phys. G **38**, 1517 (2004).

[24] R.V. Gavai, D. Kharzeev, H. Satz, G. Schuler, K. Sridhar and R. Vogt, Int. J. Mod. Phys. A **10**, 3043 (1995); G.A. Schuler and R. Vogt, Phys. Lett. B **387**, 181 (1996).

[25] B.L. Combridge, Nucl. Phys. B **151**, 429 (1979).

[26] R. Vogt, Z. Phys. C **71**, 475 (1996); Heavy Ion Phys. **17**, 75 (2003).

[27] C.W. deJager, H. deVries, and C. deVries, Atomic Data and Nuclear Data Tables **14**, 485 (1974).

[28] D. Kharzeev, E.M. Levin and M. Nardi, hep-ph/0212316; L. Húlthen and M. Sagawara, in *Handbüch der Physik*, **39** (1957).

[29] A.D. Martin, R.G. Roberts, and W.J. Stirling, and R.S. Thorne, Phys. Lett. B **443**, 301 (1998).

[30] M. Glück, E. Reya, and A. Vogt, Z. Phys. C **53**, 127 (1992).

[31] K.J. Eskola, V.J. Kolhinen and P.V. Ruuskanen, Nucl. Phys. B **535**, 351 (1998).

[32] K.J. Eskola, V.J. Kolhinen and C.A. Salgado, Eur. Phys. J. C **9**, 61 (1999).

[33] L. Frankfurt, V. Guzey and M. Strikman, arXiv:hep-ph/0303022.

[34] H.L. Lai *et al.*, Eur. Phys. J. C **12**, 375 (2000).

[35] G.T. Garvey and J.C. Peng, Phys. Rev. Lett. **90**, 092302 (2003).
[36] V. Emel'yanov, A. Khodinov, S.R. Klein and R. Vogt, Phys. Rev. C **59**, 1860 (1999).
[37] R. Vogt, Nucl. Phys. A **700**, 539 (2002).
[38] R. de Cassagnac (PHENIX Collaboration), J. Phys. G **30**, S1341 (2004).
[39] H. Pereira (PHENIX Collaboration), proceedings of Strangeness in Quark Matter, Sept. 2004.

FIGURES

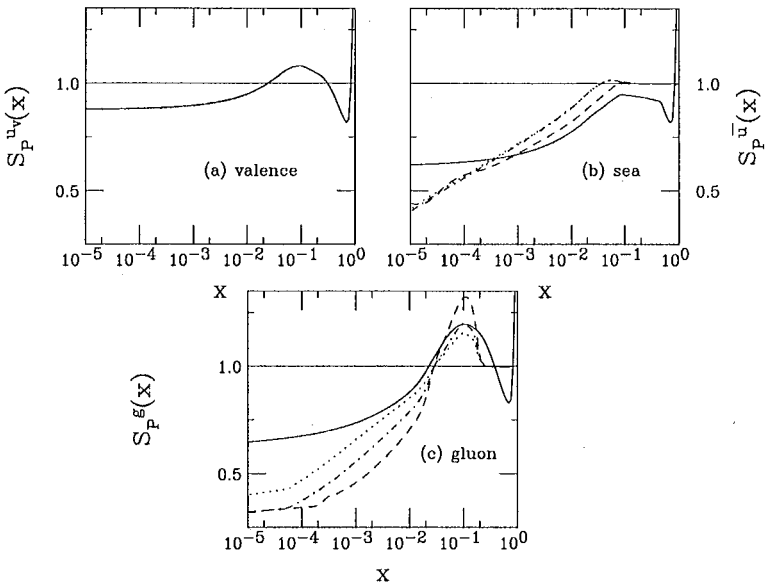

FIG. 1. The shadowing parameterizations are compared at the scale $\mu = 2m_c = 2.4$ GeV. The solid curves are EKS98, the dashed, FGSo, dot-dashed, FGSh, and dotted, FGSl.

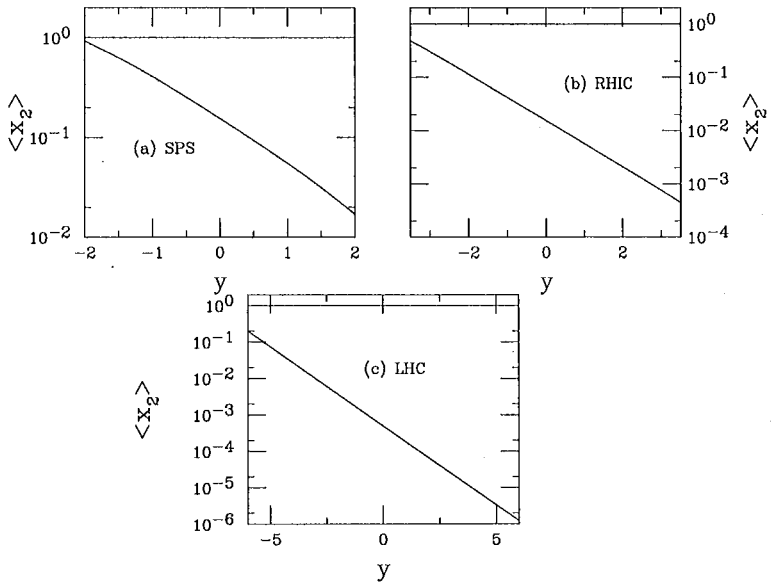

FIG. 2. We give the average value of the nucleon momentum fraction, x_2, of J/ψ production in pp collisions as a function of rapidity for (a) the CERN SPS with $\sqrt{S} = 19.4$ GeV, (b) RHIC with $\sqrt{S} = 200$ GeV and (c) the LHC with $\sqrt{S} = 6.2$ TeV.

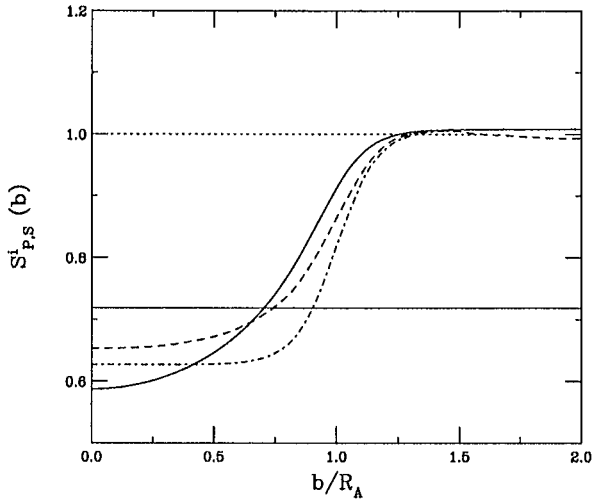

FIG. 3. The WS (dot-dashed) and ρ (solid) inhomogeneous shadowing parameterizations are compared to the inhomogeneous FGS shadowing parameterization (dashed) at the same value of the homogeneous ratio, indicated by the horizontal solid line.

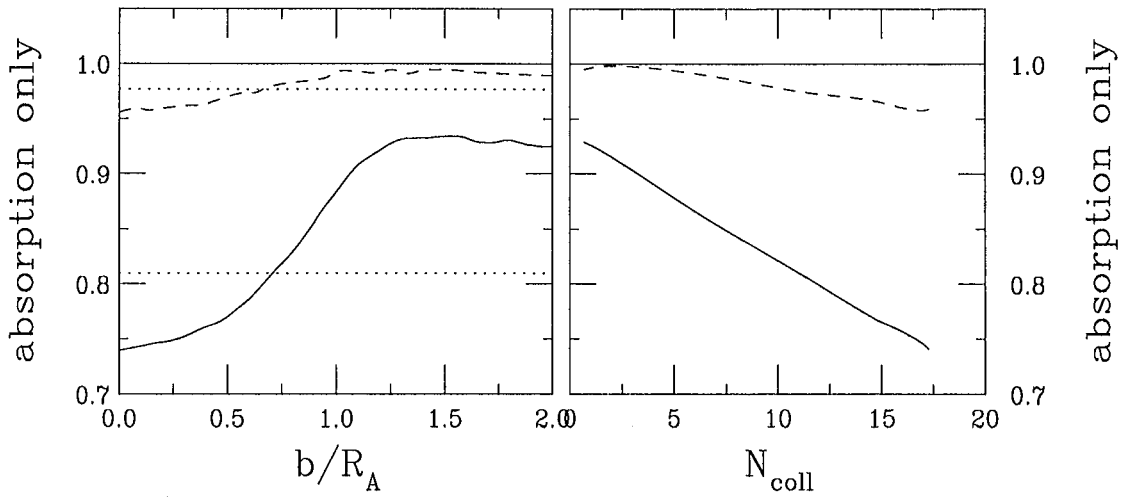

FIG. 4. The J/ψ dAu/pp ratio for absorption alone with $\sigma_{\rm abs} = 3$ mb as a function of impact parameter (left-hand side) and as a function of the number of nucleon-nucleon collisions, $N_{\rm coll}$, (right-hand side) for a constant octet (all y), solid, and singlet ($y = -2$), dashed. The homogeneous results are indicated by the dotted lines.

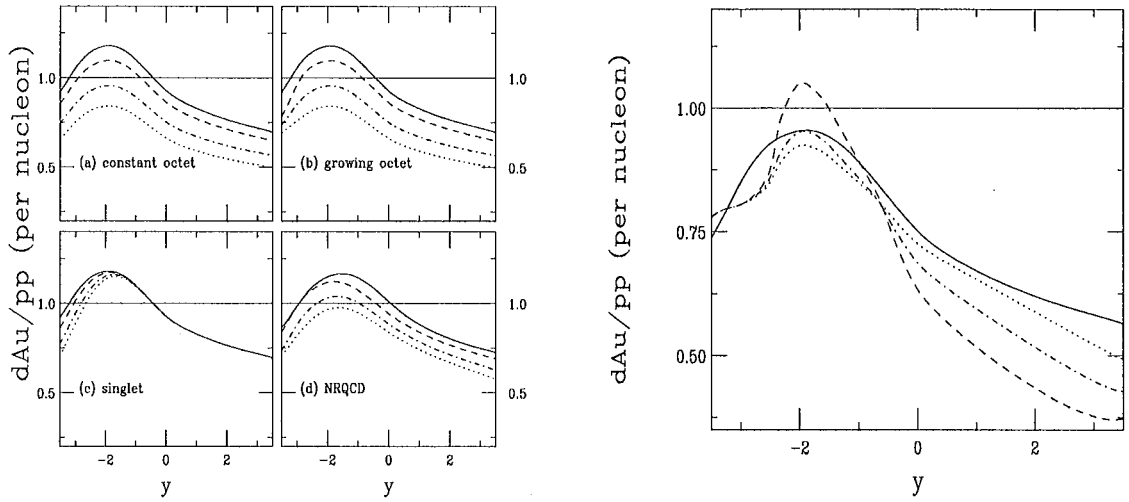

FIG. 5. Left-hand side: The J/ψ dAu/pp ratio with EKS98 at 200 GeV as a function of rapidity for (a) constant octet, (b) growing octet, (c) singlet, all calculated in the CEM and (d) NRQCD. For (a)-(c), the curves are no absorption (solid), $\sigma_{\rm abs} = 1$ (dashed), 3 (dot-dashed) and 5 mb (dotted). For (d), we show no absorption (solid), 1 mb octet/1 mb singlet (dashed), 3 mb octet/3 mb singlet (dot-dashed), and 5 mb octet/3 mb singlet (dotted). Right-hand side: The J/ψ dAu/pp ratio at 200 GeV for a growing octet with $\sigma_{\rm abs} = 3$ mb is compared for four shadowing parameterizations. We show the EKS98 (solid), FGSo (dashed), FGSh (dot-dashed) and FGSl (dotted) results as a function of rapidity.

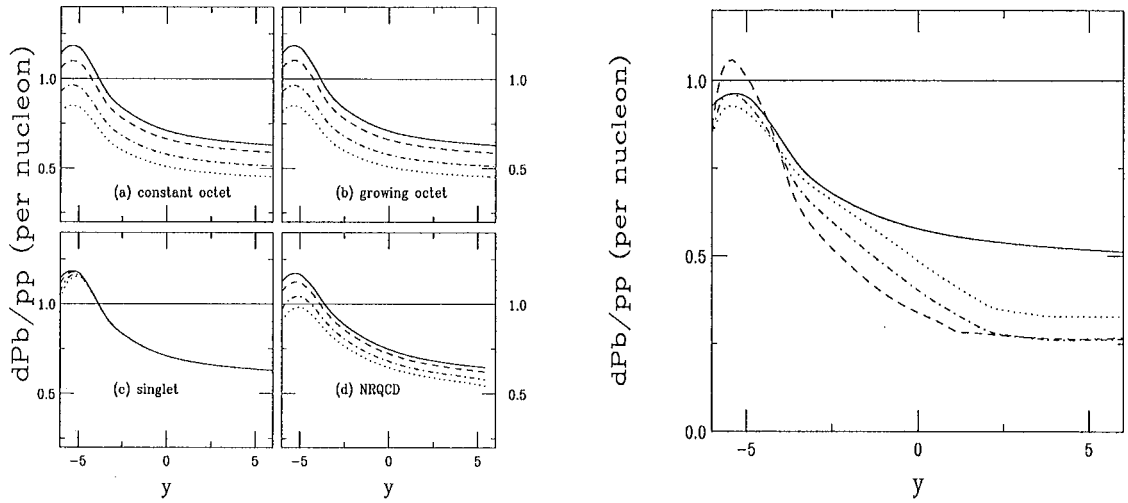

FIG. 6. Left-hand side: The J/ψ dPb/pp ratio with EKS98 at 6.2 TeV as a function of rapidity for (a) constant octet, (b) growing octet, (c) singlet, all calculated in the CEM and (d) NRQCD. For (a)-(c), the curves are no absorption (solid), $\sigma_{\rm abs} = 1$ (dashed), 3 (dot-dashed) and 5 mb (dotted). For (d), we show no absorption (solid), 1 mb octet/1 mb singlet (dashed), 3 mb octet/3 mb singlet (dot-dashed), and 5 mb octet/3 mb singlet (dotted). Right-hand side: The J/ψ dAu/pp ratio at 200 GeV for a growing octet with $\sigma_{\rm abs} = 3$ mb is compared for four shadowing parameterizations. We show the EKS98 (solid), FGSo (dashed), FGSh (dot-dashed) and FGSl (dotted) results as a function of rapidity.

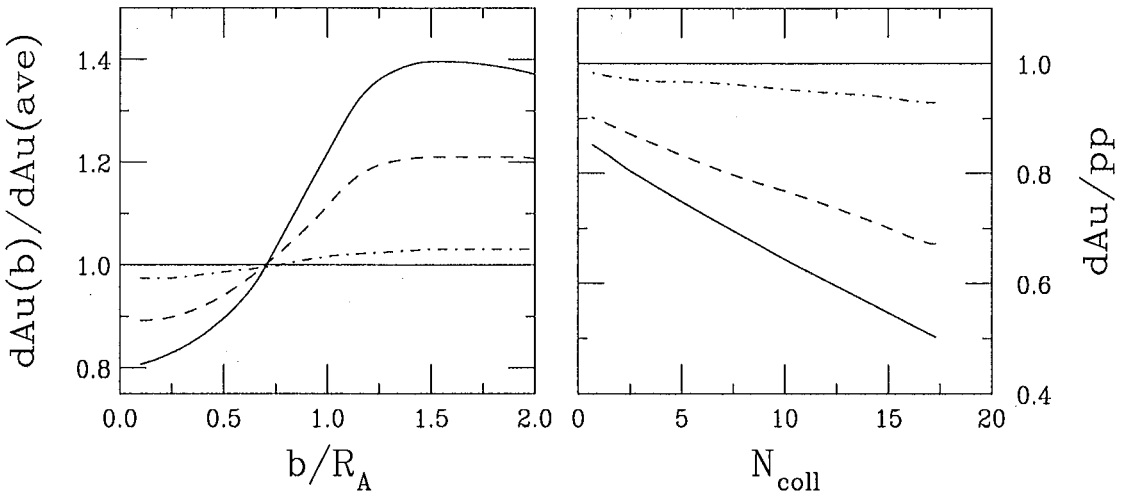

FIG. 7. Left-hand side: The J/ψ ratio dAu(b)/dAu(ave) as a function of b/R_A. Right-hand side: The ratio dAu/pp as a function of $N_{\rm coll}$. Results are shown for $y = -2$ (dot-dashed), $y = 0$ (dashed) and $y = 2$ (solid) at 200 GeV for a growing octet with $\sigma_{\rm abs} = 3$ mb and the EKS98 parameterization.

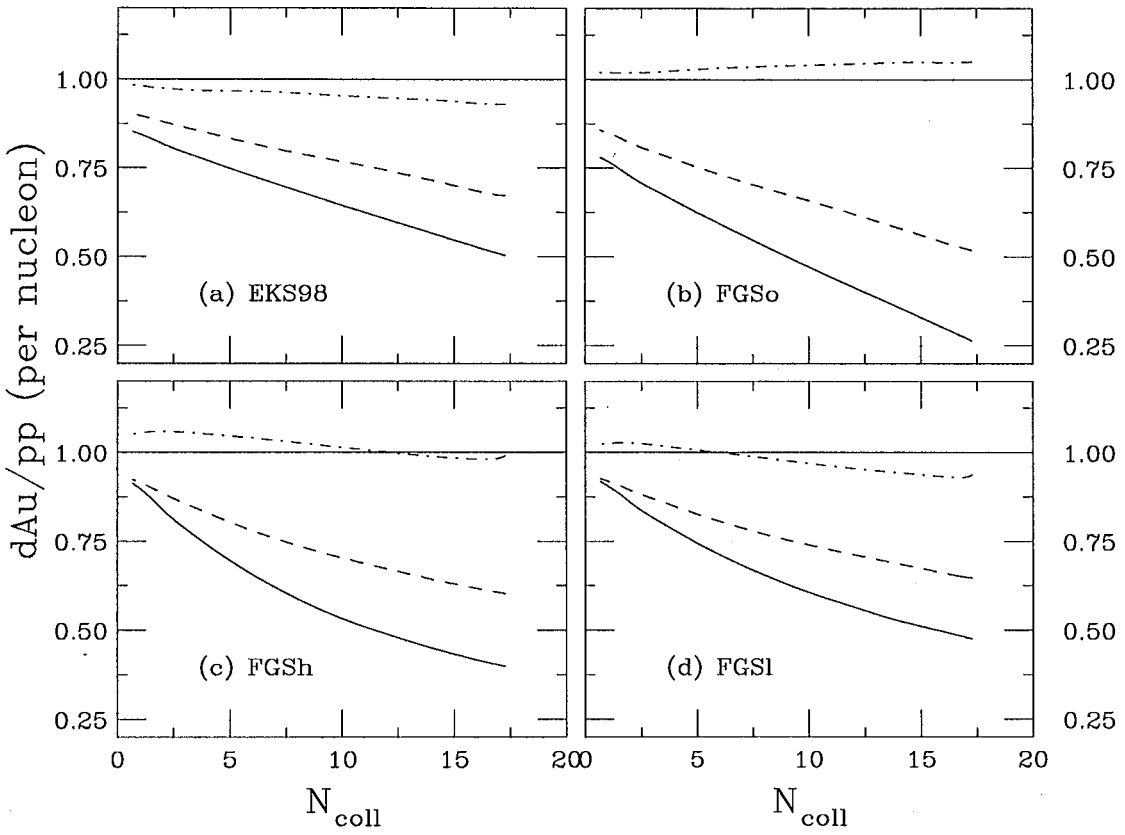

FIG. 8. The ratio dAu/pp as a function of $N_{\rm coll}$ for the EKS98 (a), FGSo (b), FGSh (c) and FGSl (d) shadowing parameterizations. The calculations with EKS98 and FGSo use the inhomogeneous path length parameterization while that obtained by FGS is used with FGSh and FGSl. Results are given for $y = -2$ (dot-dashed), $y = 0$ (dashed) and $y = 2$ (solid) at 200 GeV for a growing octet with $\sigma_{\rm abs} = 3$ mb.

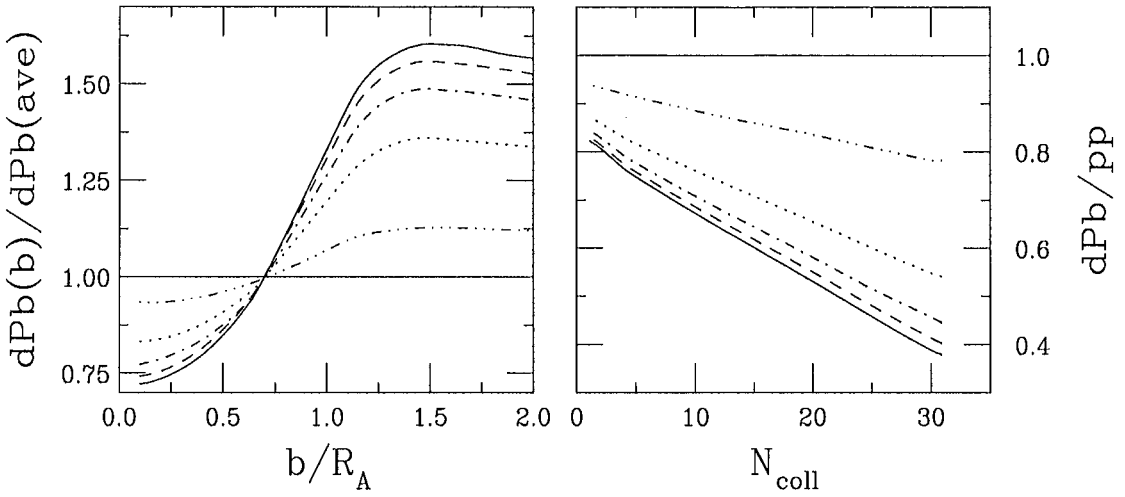

FIG. 9. Left-hand side: The J/ψ ratio dPb(b)/dPb(ave) as a function of b/R_A. Right-hand side: The ratio dPb/pp as a function of $N_{\rm coll}$. Results are shown for $y = -4$ (dot-dot-dot-dashed), $y = -2$ (dotted), $y = 0$ (dot-dashed), $y = 2$ (dashed) and $y = 4$ (solid) at 6.2 TeV for a growing octet with $\sigma_{\rm abs} = 3$ mb and the EKS98 parameterization.

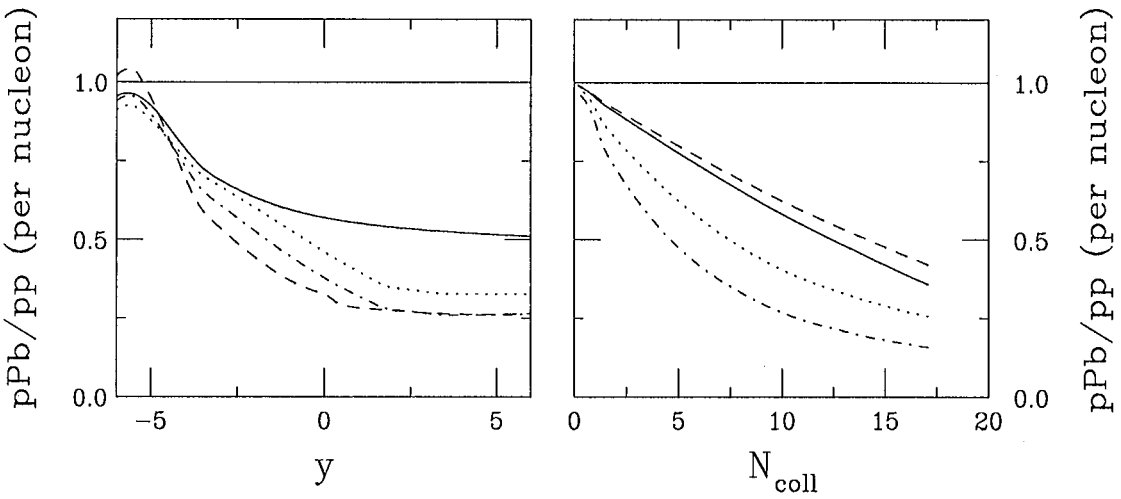

FIG. 11. Left-hand side: The ratio pPb/pp at 8.8 TeV as a function of rapidity for the EKS98 (solid), FGSo (dashed), FGSh (dot-dashed) and FGSl (dotted) shadowing parameterizations with a 3 mb octet absorption cross section. Right-hand side: The $N_{\rm coll}$ dependence for EKS98 ($y = 4$, solid curve and $y = 0$, dashed curve) and FGSh ($y = 4$, dot-dashed curve and $y = 0$, dotted curve).

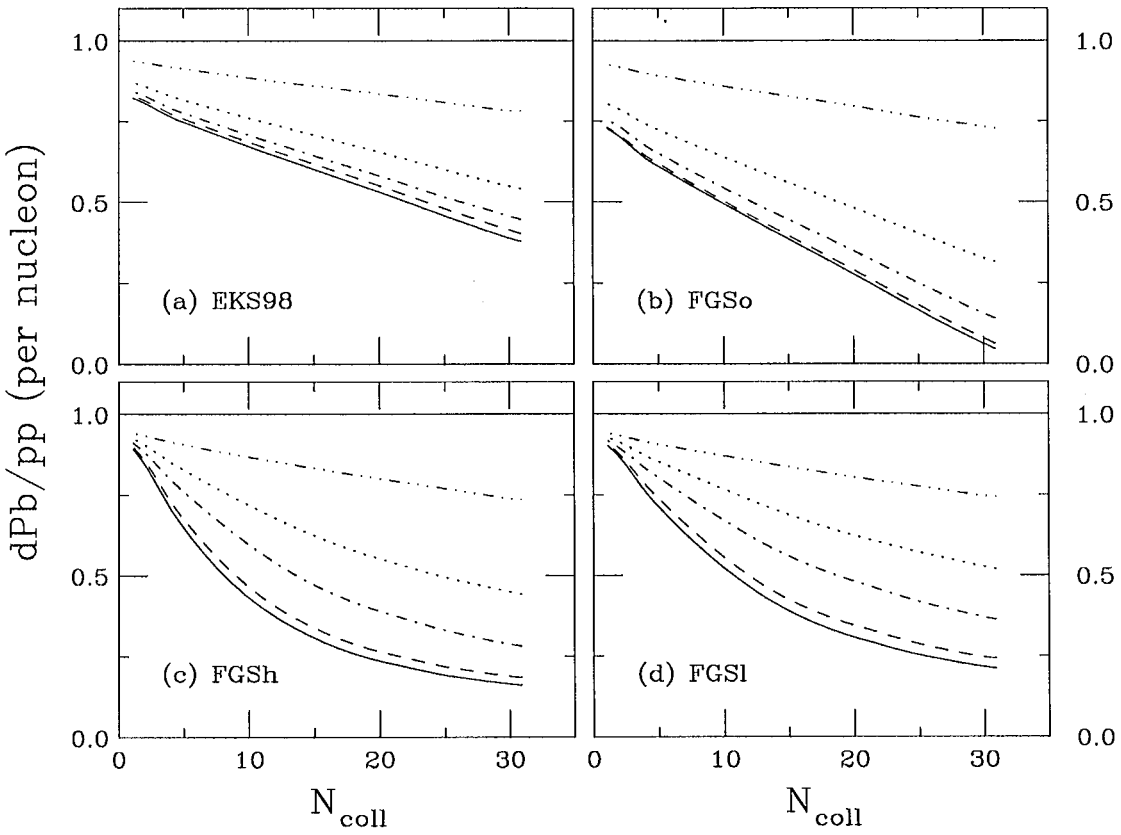

FIG. 10. The ratio dPb/pp as a function of $N_{\rm coll}$ for the EKS98 (a), FGSo (b), FGSh (c) and FGSl (d) shadowing parameterizations. The calculations with EKS98 and FGSo use the inhomogeneous path length parameterization while that obtained by FGS is used with FGSh and FGSl. Results are given for $y = -4$ (dot-dot-dot-dashed), $y = -2$ (dotted), $y = 0$ (dot-dashed), $y = 2$ (dashed) and $y = 4$ (solid) at 6.2 TeV for a growing octet with $\sigma_{\rm abs} = 3$ mb.